International Journal of Advanced Technology in Mechanical, Mechatronics and Materials (IJATEC)

Vol. 03, No. 1 (2022) 1-17

Institute for Research on Innovation and Industrial System (IRIS)

Power Production and Drag of Autorotating Cross Cylinder Turbine Models

David J. Foote[a], Rachmadian Wulandana[a*], Seth Pearl, Nataniel Ilyayev

[a]*Mechanical Engineering Program, State University of New York (SUNY) New Paltz, 1 Hawk Drive, New Paltz, NY 12561, USA*

Abstract. The autorotation phenomena of bladeless symmetric objects exposed to fluid flow have promised power generation from the kinetic energy of natural water and air currents. Our past experiments on bladeless turbine models suggest non-linear correlation between the flow speed and power production. This report explores factors such as flow obstacles and turbine's position that may affect the power generation of such turbines at Reynolds numbers around 10,000 to 50,000. Using a custom-made water flow tank, the power production and generated drag forces of 3D-printed bladeless turbine models were examined under various conditions of flow. Initially in previous research, analysis was conducted regarding the design of the turbine without extensive detail regarding flow. The following research examines how flow characteristics affect power generation. Results indicate the significant effect of flow straightener and flow perturbation to the power production. Additionally, the effects of turbine infill density and flow speed on the generated drag and measured rotation-per-minute (RPM) are reported. The minimal effects from the turbine's weight and position in the water flow on the power production require further exploration.

Keywords: autorotation; hydrokinetic; bladeless turbines; renewable energy

DOI: 10.37869/ijatec.v3i1.52
Received 28 December 2021; Accepted 5 March 2022; Available online 30 April 2022

1. Introduction

Fossil fuels have provided us with the most electricity compared to other energy resources, however the negative effects of coal mining and oil production on the environment are devastating and irreversible. While the cost of fossil fuels is historically been low, renewable resources, such as water flow, wind, ocean current, solar energy, biomass, etc. have provided alternatives that are clean and environmentally friendly. Though the technology is still developing, renewable resources are being increasing seen as the future power of civilization. Recent report by International Energy Agency (IEA) indicates persistent growth of global demand of renewable energy from 27% in 2019 to 29% in 2020 despite of the COVID-19 pandemic [1]. Hydrokinetic energy harvesting systems that target available kinetic energy of natural water streams and ocean tidal have become attractive choice of renewable energy resource due to its minimum environmental impact. Unlike hydropower systems that demand large areas and massive infrastructure, hydrokinetic systems rely on natural setup of the water current. The hydrokinetic energy harvesting system typically consists of a generator, typically a Permanent Magnet Synchronous Generator (PMSG), a power converter, and either batteries or grid-tie connection systems [2]. Its simple setup attracts utilization of this system for electrifying of remote areas. Assessment on the real application of hydrokinetic renewable energy harvesting for isolated areas indicated promising results. Areas of

*Corresponding author: wulandar@newpaltz.edu
ISSN: 2720-9008

studies include the Mahakam river in East Kalimantan, Indonesia[3], Kapuas Hulu, West Kalimantan, Indonesia [4], an inlet canal for a hydropower plant in Indonesia [5], villages in Sarawak, Malaysia [6, 7], Niah river, also in Sarawak [8], as well as various places in Malaysia [9–11], along the coastal region of Bangladesh Inland Water Transport Authority[12], East District of Sikkim, India[13], along U-Tapao river of southern Thailand[14], Nigeria[15–17], regions in South Africa [18, 19], Amazon region in Brasil [20], Cozumel channel in Brasil [21], etc. These studied underlines the high potential of hydrokinetic systems that are largely untapped. Susilowati et al. suggested that various micro-hydroelectric technologies can replace the existing state-supplied diesel generators used by communities along Mahakam river in East Kalimantan, Indonesia[3]. In fact, the total hydrokinetic potential capacity in Indonesia has been reported to be approximately 144 MW, but only 2.6 MW has been installed in 2014[22]. In the United States, the average energy harvesting potential from hydrokinetic systems applied on all rivers is estimated to be 12.6 GW annually with minimum impact on aquatic life [23]. These studies suggest the importance of research and development in this area.

Our research enterprise has been focused on creative designs of vortex-induced autorotating turbines applicable for hydrokinetic energy harvesting. Unlike traditional turbines that rotate due to the drag and lift forces on the blades, the rotation and vibration of vortex-induced turbines are caused by the vibration of vortex-shedding that trails behind the turbines. The vortex-induced vibration (VIV) of objects exposed to fluid flow are ubiquitous in nature and often need to be avoided for man-made structures due to its catastrophic consequences. However, recent attempts to harvest energy from vortex-induced vibration become attractive for renewable energy conversion due to its promising features such as scalability, modality, safety, and affordability [24–26]. The proper autorotation of a body corresponds to the existence of one or more stable positions at which the fluid flow exerts zero torque on the resting body [27, 28]. Accordingly, "a sufficiently strong initial impulse is required before the fluid flow can sustain a continuous spinning of the body"[27]. Autorotating mechanism of blunt bodies exposed to fluid flow can be categorized as one of type of vortex-induced vibration[29].

Past experimentation on various turbine designs has been made possible by a custom-made closed-loop water flume equipped with a transparent open channel, a 3-hp centrifugal pump and a Variable Frequency Drive to control the pump's speed [30]. This current report further explores the energy harvesting potential of bladeless cross-cylinder turbine designs proposed by Araneo and Foote[31, 32]. The bladeless feature is attractive as it can reduce the harm imposed on marine life. The selected turbine shape in this study represents a merging of two short cylinders arranged orthogonally. The design is motivated by a well-studied autorotation phenomenon demonstrated by mini Delrin plastic cylinders exposed to water flow at medium Reynolds number. In this work, short cylinders with diameter-to-length ratio of unity show autorotation for a range of medium Reynolds number [33]. In this experiment, the short plastic cylinder samples demonstrate either stagnation, random oscillation, periodic oscillation, or autorotation. The preference mode depends on the non-dimensional inertia and Reynolds numbers. The autorotation phenomena occur for samples with non-dimensional inertia of ~ 0.2 that are exposed to flow with Reynolds number of around $\sim$3000 to 4500. When the short cylinders are in stagnation or random oscillation, the long axis would be parallel to the flow direction. Since the current turbine design is a combination of two short cylinders arranged perpendicular to one another, it was expected that the model would keep rotating as one cylinder would be in the stagnation (stable) configuration while the other would be orthogonal from that (unstable). We also hypothesize that the flat circular areas are expected to harness enough shearing forces and torque to cause rotation. On the other hand, our cross-cylinder turbine model has also been inspired by results on the autorotation of polygonal shapes exposed to air flow [34]. In this study, it was discovered that polygonal prisms having three and four sides demonstrate greater rotations than that with larger number of sides.

There are three types of turbine systems used for hydrokinetic energy harvesting: axial (horizontal), vertical, and cross flow [35]. These classifications have to do with where their axis of rotation is with respect to the direction of fluid flow. The current project will involve studying vertical axis turbines (axis of rotation perpendicular to the direction of flow) due to its easier test setup when compared to axial turbines (axis of rotation parallel to the direction of flow) and having

a more popular interest of study when compared to cross flow turbines (axis of rotation perpendicular in the horizontal direction to the direction of flow)[36].

This paper reports results from experiments using the water tank for power, drag and RPM experiments. First, we will describe the 3D-printed turbine models that are used in the subsequent experiments. Following that, an overview of each of the experiments is presented. Overall, the leading purpose of the experimentation conducted is to better understand and quantify design criteria for autorotating turbines that can later be scaled and applied in broader engineering applications.

2. Materials and Methods

The selected 3D-printed turbine model, named cross cylinder model, used in this project represents an orthogonal overlapping of two congruent cylinders that are pinched at their centroids[31]. The overall shape has an edge-to edge distance, which would be referred to as diameter of 5 cm. The overall dimension of the turbine is 5x5x5 cm^3. The turbine was 3D-printed using polylactic acid (PLA) material. The printing was executed using 10% infill parameter, which resulted in a total mass of 30.5 gram. The volume of the model is calculated in SolidWorks to be 128.74 cm^3. The advantage with using PLA as the material composition for the 3D-printed turbines involves cost and minimum environmental impact. The price of acrylonitrile butadiene styrene (ABS) is twice that of PLA for the same amount of material, yet its properties are comparable to that of ABS. From an environmental standpoint, PLA is a biodegradable polymer [4], meaning that it is not poisonous and will not be harmful to the surrounding marine life if consumed. A 2-mm stainless steel shaft is pressed fit into the point where the circumferential surfaces of the two cylinders intersect. The stainless-steel shaft then is coupled with the short shaft of a small 0.5 V DC motor using a rigid plastic tube. Furthermore, the DC motor is enclosed in a custom-made 3D-printed casing that can be lowered into the water stream. The telescoping mechanism allows the shaft exposed to water to be made as short as possible to reduce bending caused by the fluid force acting on the turbine model. During the tests, the motor case and the turbine model are secured on a pair of perforated-slotted angle bars (an L-section) that are placed across the top of the observation chamber. Furthermore, the angle bars are also secured using bolts on similar perforated-slotted angle bars attached on the outside of both walls of observation chamber. The turbine model, 3d-printed the fixture for the motor enclosure, and the coupling for the turbine's shaft are shown in Figure 1 below.

Two sets of experiments are reported here; power and drag experiments. In all of the experiments, the turbine was sustained 3" below the water surface in a 15x15x60 cm^3 transparent chamber made of plexiglass with top opening. All of the experiments were conducted using a custom-made closed loop flow tank available in Thermal Fluid Lab of the State University of New York (SUNY) New Paltz campus, as shown in Figure 2 below. The flow tank is equipped with centrifugal pump capable of delivering 1200 gph of flow rates which provides a maximum of 60 cm per second of average flow speed through a 15x15x60 cm^3 transparent observation chamber [30]. This maximum flow speed target was based on a similar commercial flow tank available in Montclair State University in New Jersey [31]. The rotation of the pump propeller can be finely controlled using a commercial Variable Frequency Drive (VFD). In the experiment, factors to be varied include flow velocity, turbine's position relative from the centerline, and the presence of a flow straightener.

The power experiment is focused on the effects of Reynolds numbers, flow conditions, and turbine relative position to the centerline of the flow on the power generation. The water flow is conditioned by the presence of a 3d-printed flow straightener placed upstream the turbine. The flow straightener, shown in Figure 1 (a), is a 15x15x5 cm^3 plastic block furnished with 144 holes, each is about 1-cm in diameter. The flow straightener is expected to provide straight, less-turbulent, uniform flow impacting the turbine [30]. Past experiments using a commercial closed-loop water tank available in Montclair State University showed promising energy harvesting results for the cross-cylinder models [31, 32]. In this past works, we employed a digital multi-meter but the data was recorded manually. In the current setup, the voltage and current data were collected continuously using Dawson Digital Multimeter with USB interface over a 20 second interval (sampling frequency of 3 Hz). The multi-meter is shown in Figure 1 below. The continuous data collection allows further analysis in Excel. Absolute values of voltage and current were taken, then

the averages of each was calculated. And the power production was calculated using Ohm's Law. Additionally, the continuous data allows us to compute the time period when the turbine produces non-zero current and voltage as well as the number of "flips", where the data change signs from positive to negative. The number of "flips" reflects how many times the turbine changes its rotation or oscillation from one direction to other direction. From the continuous current and voltage data, the maximum values can be determined and those are used for the maximum potential generated power. The turbine's efficiency is defined as the ratio of the average power production to the maximum possible power.

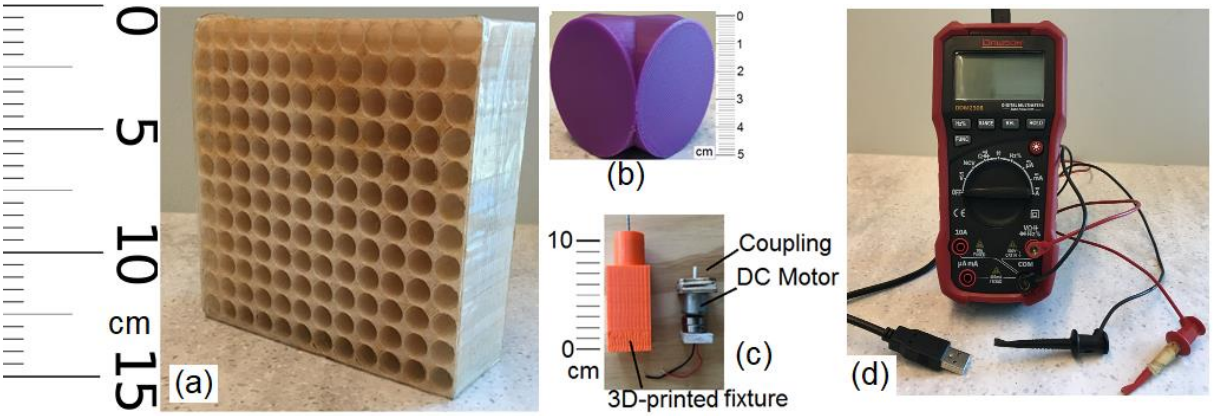

Figure 1. The 3d-printed flow straightener (a), turbine model (b), fixture for DC motor (c), and digital multimeter (d) used in the experiments

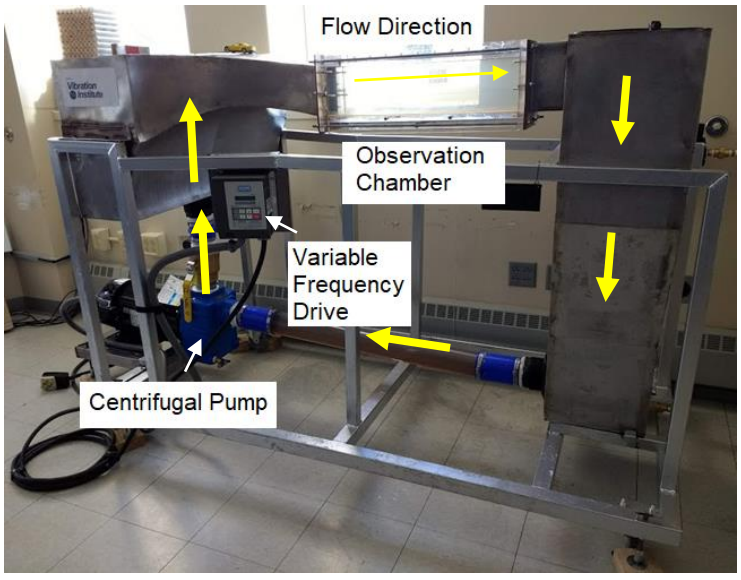

Figure 2. The custom-made water flow tank used in the experiments is equipped with a 3-hp centrifugal pump and variable frequency drive. The yellow arrows mark the water direction.

To measure the drag force during the drag experiments, a force sensor from Vernier [37] was used. The continuous data of the force exerted by the turbine was recorded at a sampling rate of 1 Hz using Vernier Graphical Analysis software available online. To achieve this objective, a 3D-printed shaft adapter at a fixed water depth of 6 cm long was designed to rigidly hold the turbine model. The fixture can be examined in Figure 4 below. The rotation-per-minute (RPM) of the turbine was observed manually using an infrared tachometer (a non-contact tachometer and counter by Reed Instruments). Here, a 0.5x0.5-cm^2 reflective tape was placed on one of turbine's flat surface to serve as the infra-red target. The resolution of the tachometer is 0.1 RPM for measurement between 2 to 1000 RPM and its sampling time is 0.5 seconds. Also, a telescoping fixture was fabricated to allow various depth of turbine's placement under the water. The fixture was made by two PVC pipes drilled with 2 cm hole- to-hole spacing, 3D printed turbine shaft

adapter system, 3D-printed pipe clamp and two 2-inch-long hex bolts to secure the fixture to the flow tunnel rails. The telescoping feature allows the investigation of the effect of water depth in the flow tank. The shaft adapter system utilizes a pen barrel and two 3D-printed parts. One that connects to the turbine shaft and to the pen barrel, and one that connects the barrel to the PVC pipe. This pen barrel system was developed to increase the rigidity of the 2mm fitted shaft without producing unnecessary drag of the ½ inch PVC pipe. The set up for the RPM experiment can be seen below in Figure 3. Unlike the setup for the power experiment, here a 2-mm stainless steel bearing must be carefully press-fitted onto the point where the metal shaft was inserted on the turbine. Hence, for the RPM measurement, the turbine is let to spin while the shaft is fixed.

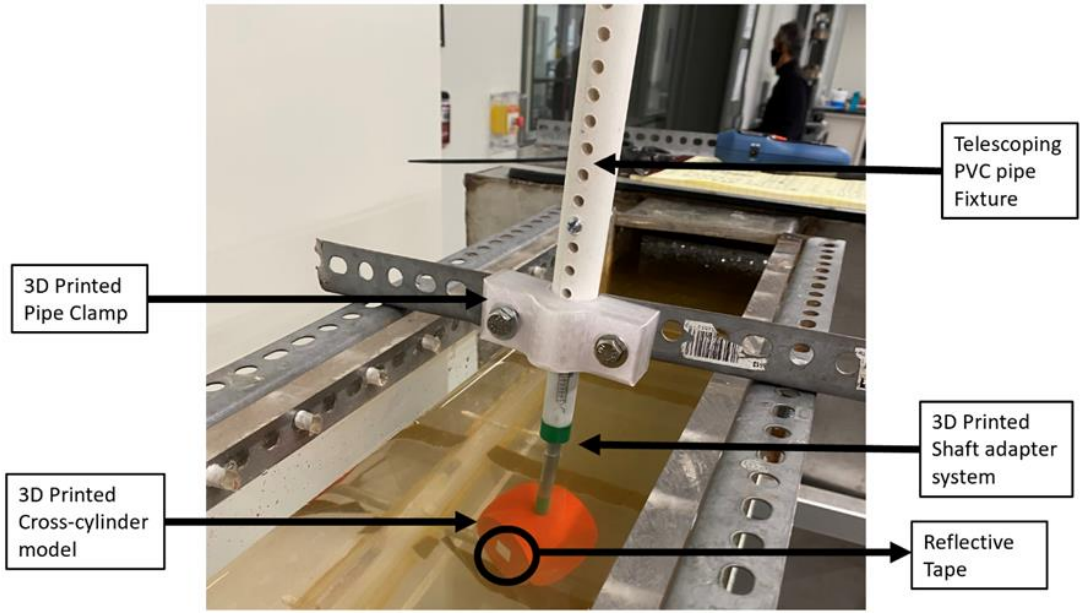

Figure 3. Experiment setup for RPM measurements of the turbine models that includes a telescoping mechanism made of perforated PVC pipe

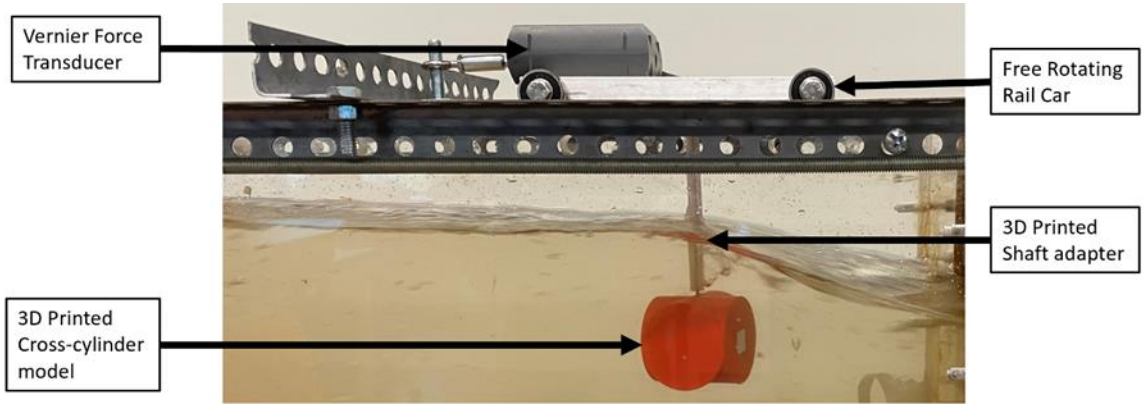

Figure 4. Experiment setup for drag measurements of the models involving a force sensor placed on aluminum block with smooth rollers

The power experiments are conducted for the following scenarios:

1. Symmetric flow – For this case, the center of the turbine model is placed at the middle of the channel (see Figure 5 below). Assuming that the flow profile is symmetrical about the middle axis of the observation chamber, this case exposes the turbine on the maximum velocity value. While the velocity profile in the chamber has not been visually evaluated, three-dimensional computational fluid dynamics (CFD) modeling of the water inside the observation chamber indicates possible near fully developed symmetrical profile in the chamber [30].
2. Asymmetric flow – In this case, the center of the turbine model is placed approximately 5 cm from the chamber wall or 2.5 cm from the center of the chamber (see Figure 5 below). The

selected distance is the most optimum utilization of the total chamber clean width of 15 cm. This case is selected to study the effects of eccentricity, the deviation of the model position from its symmetric configuration on the autorotation and power production.

3. With flow straightener – In this case, the upstream flow is blocked by the 3D-printed flow straightener. The device is pressed fit against the chamber wall at the end of the converging channel. The 144 circular holes of the flow straightener are arranged parallel with the flow direction and they are expected to provide uniformly horizontal flow into the observation chamber. The horizontal flow is expected to promote autorotation better than flow with less uniform pattern.

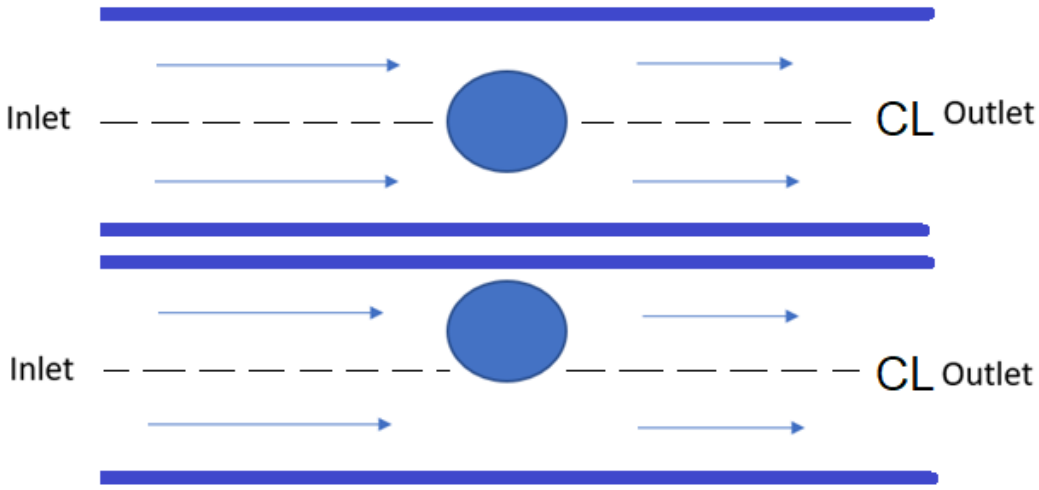

Figure 5. This cartoon shows the top view of the symmetric case (top) versus asymmetric case (bottom) of turbine's placement in the water flow

The power experiment was conducted at water's average speed of 60 to 70 cm per second. For the RPM and drag experiments, the average water flow speed was varied between 20 and 60 cm per second. For the drag experiments, we use three turbine models with different masses but the same dimension. The mass variation is achieved by incorporating infill parameters used in the 3d-printing; 10%, 40%, and 80%. The effects of turbine's depth on the RPM are evaluated by experimenting for three different depths: 5 cm, 7 cm, and 9 cm. A force sensor was used to measure the force exerted on the model; a 60 second time interval was recorded using the Vernier Graphical Analysis software. The mean drag force (F) was recorded and interpreted for six flow speeds. Using equation 1, the coefficient of drag (C_D) for each model was calculated. Here, A is the frontal cross-sectional area of the turbine normal to the flow direction ($A = 25\ cm^2$), V is the average flow speed, and ρ is the water's density of 998 kg/m^3. The Reynolds number was calculated using equation 2, where ρ is the density of water, μ is the dynamic viscosity of water taken at 0.001 Pa.s, D is the diameter of the turbine of 5 cm, and V is the average water speed. The tachometer senses a full rotation of the model when it registers the reflective tape. The time in between the rotations resulted in a rotational speed measurement. A 60 second sample was recorded, the minimum, maximum and mean RPM data was recorded at 6 water flow rates and 3 water depths, 18 data sets were recorded for each model.

$$C_d = \frac{F}{0.5A\rho V^2} \tag{1}$$

$$Re = \frac{\rho DV}{\mu} \tag{2}$$

3. Results and Discussions

The power and drag experiments yield various results in terms of Reynold numbers. From the power experiment, which focuses on the power production, the results can be summarized as:

- Average power production versus Reynolds number
- Maximum possible power versus Reynolds number
- Turbine efficiency versus Reynolds number
- Number of "flips" versus Reynolds number and
- Maximum production time versus Reynolds number

These results display the effects on turbine's position with respect to the flow profile and the presence of flow straightener on these parameters. The symmetric configuration represents the configuration when the turbine is positioned at the local maximum velocity (middle of the channel), while the asymmetric configuration is achieved by positioning the turbine close to the wall, moved away from the center of the velocity profile. The presented results below show that the flow straightener and the symmetric configuration generally improve the power production by the turbine.

From the drag experiment, which focuses on the measurement of drag forces, results of rotation-per-minute (RPM) and drag coefficient are presented. Here, the effects of turbine's weight and depth on the drag are studied. The weights are varied by utilizing different in-fill parameters during the printing of the models. To study the effects of depth, the turbine is tested for various flow speed as it is placed 5 cm, 7.5 cm, and 9 cm below the water surface.

3.1 Results from Power Experiments

Figures 6 presents the produced averaged power produced by turbines in the flow with and without the upstream flow straightener. The average power is the product of time-averaged voltage and current data taken for the observation period. For each case, symmetric and asymmetric setups were analyzed.

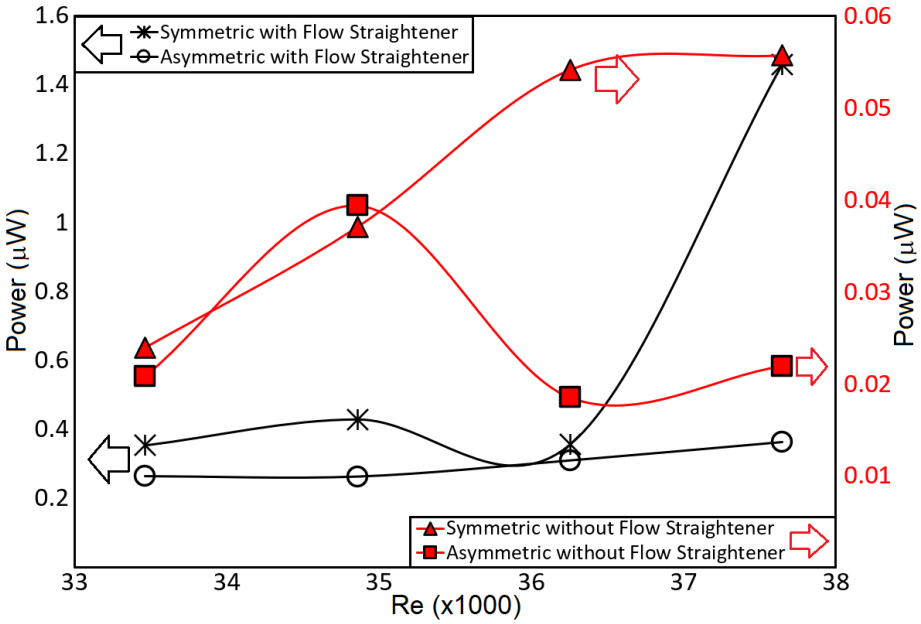

Figure 6. Average Power Production versus Reynold numbers for the cases with flow straightener (black lines with circle and star markers using left y-axis) and cases without flow straightener (red lines with triangular and square markers using right y-axis)

Results indicate that the average power produced in the presence of flow straightener are much higher than the case without the flow straightener. Hence, in the graph, the cases with flow straightener (black lines marked with star and circle) are plotted using the left y axis, while the cases without flow straightener are plotted using the right y-axis (red lines marked with red triangles and squares). The symmetric case with flow straightener is shown to yield more than 1.4 μW at maximum Reynold number around 37,000. At average, the cases with the flow straightener produce about 0.2 to 0.4 μW for the studied range of Reynold numbers. For this case, increasing the flow speed has consistently caused the increase in power. Also, for the case with flow straightener,

the symmetric cases seem to be consistently better in power production than the asymmetric cases. The power produced without the flow straightener are much less. The maximum power again is produced by the symmetric case, but it only reaches less than 0.06 μW. The effects of flow speeds do not show consistent trend for the asymmetric case. For this case, the power initially provided increase in power up to a Reynolds number of 35,000 however suffered significant loss at higher numbers. For the symmetric case, increasing flow speed has resulted in the increase of power production but the trend is not necessarily to be linear. Unlike the case with the flow straightener, the turbine's placement does not seem to have clear impact on the power production when the flow straightener is absence. The significant increase in power production due to the flow straightener might be explained by the increase in the local velocity due to the reduced cross section area of the flow. It might be speculated as well that the holes of the flow straightener have presented parallel water jets that promote better vortex-shedding behind the turbine.

Figure 7 reinforces the results seen in Figure 6 that symmetric case is not only yields higher average power production than other cases but also allows for the highest power production possible. Again, here, due to the significant difference in the power production, the left y-axis is used for the cases with flow straightener (black lines marked with black star and circle), while the right y-axis is used for the cases without flow straightener (red lines marked with red triangle and square). It is clear on the graph that at a high Reynolds number, the case with symmetric flow with flow straightener yields maximum possible power of 9 μW , almost ten times higher than that without the flow straightener. This promising result would need to be further researched before any possible scale-up could be conducted.

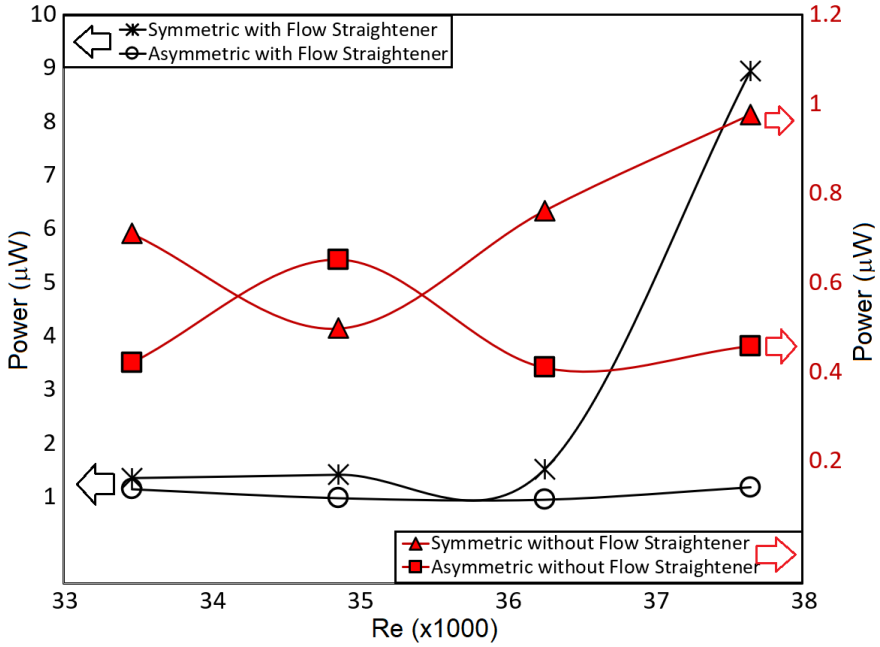

Figure 7. Maximum possible power for the cases with flow straightener (black lines with circle and star markers using left y-axis) and cases without flow straightener (red lines with triangular and square markers using right y-axis)

Figure 8 shows the efficiency of the turbine at various flow conditions. The efficiency is the ratio of the average power and the maximum possible power shown in Figures 6 and 7, respectively. In both Figures 6 and 7, it was evident that cases with flow straightener would yield the highest average and maximum possible power. Figure 8 shows that the cases with flow straightener also show much higher efficiency than the cases without flow straightener. The turbine's efficiency for the cases without flow straightener can yield 30 percent while that without the flow straightener can only yield up to ~ 8 percent. The effects of flow speeds and turbine's placement on the efficiency seem to be minimal for the case without flow straightener. It is also interesting to note that the efficiency for the symmetric case with flow straightener drops significantly at high Reynolds number where the power production was peaked. On the other hand, the efficiency for the asymmetric case with flow straightener increases with the flow speeds, although the power

production was relatively constant for this range of Reynolds numbers. This intriguing result certainly warrants further analysis in which the risks and benefits of the two flow conditions would need to be analyzed.

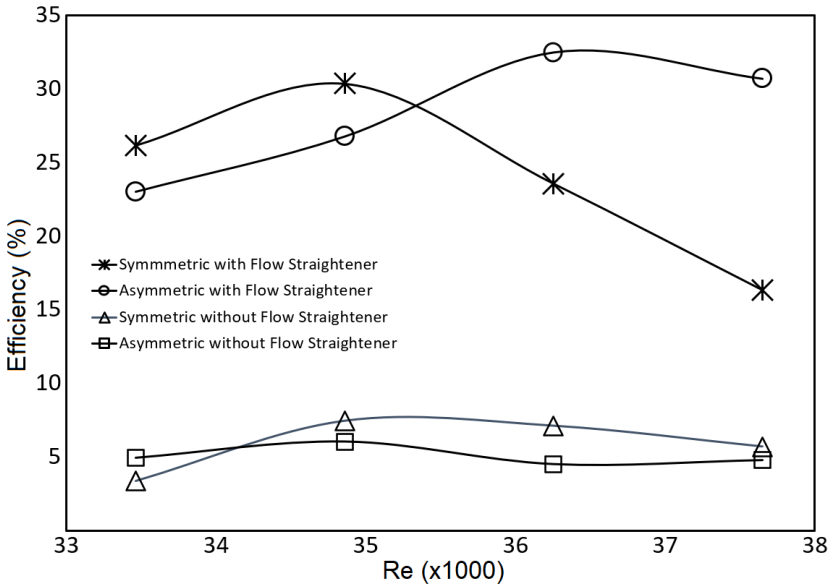

Figure 8. Efficiency of the turbine for the cases with flow straightener (circle and star markers) and cases without flow straightener (triangular and square markers)

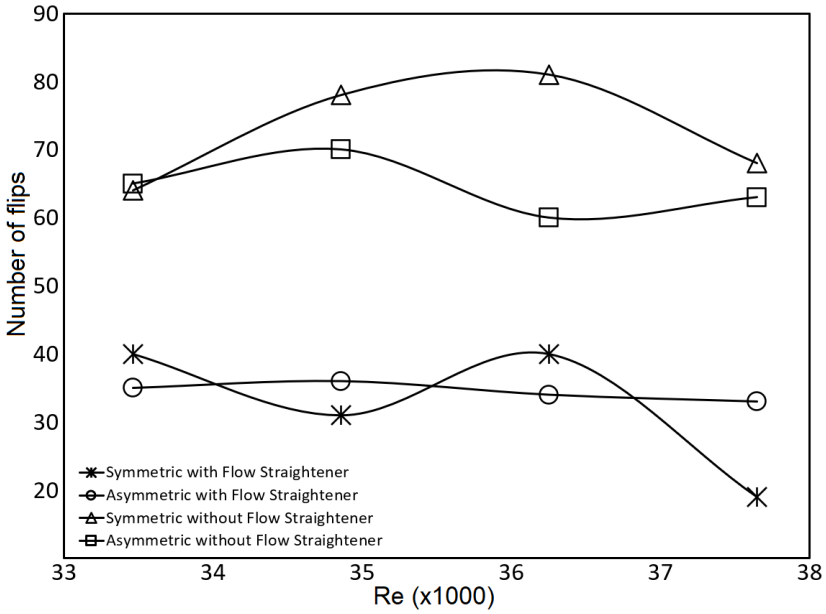

Figure 9. Number of "flips" demonstrated by turbine for the duration of 40 seconds for the cases with flow straightener (circle and star markers) and cases without flow straightener (triangular and square markers)

Figure 9 shows the number of "flips" or changing in the rotational direction demonstrated by the turbine as it gets exposed to flow for a period of approximately 40 seconds. The continuous positive and negative data of current and voltage allows us to count the number of switches from one sign to another. The high number of "flips" by the case without flow straightener indicates that high frequency of oscillation and low rotational time. This result provides confirmation that the low power production by the cases without the flow straightener can be associated with the high frequency of oscillation. As the turbine is flipping / changing direction too often, the rotation is slowed and then stopped when the turbine flips leading to a decrease in power production. This Figure 9 also suggests the minimum effects by the turbine's placement on the oscillation frequency of the turbine. It can be noted as well that, for the cases of flow with flow straightener, the graphs are relatively constant with respect to the increase in the Reynolds numbers. While for the case

without flow straightener, the Reynolds numbers seem to have inconsistent effects on the number of flips. For the symmetric case with flow straightener, the curve indicates a local maximum for the given range of Reynolds numbers. The association of maximum oscillation frequency of the turbine with a critical Reynold number needs further exploration.

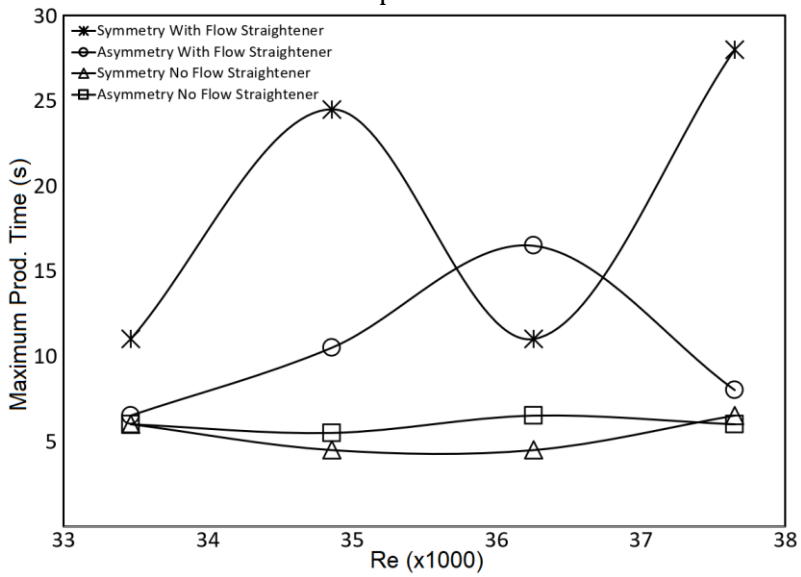

Figure 10. Maximum Production Time demonstrated by turbine for the duration of 40 seconds for the cases with flow straightener (circle and star markers) and cases without flow straightener (triangular and square markers)

Figure 10 depicts the maximum time demonstrated by the turbine to produce power. The data recording enables us to find the longest time spent by the turbine to continuously produce either current or voltage without switching the signs or flips during the 40-second observation windows. For the cases where the flow straightener is not used, the maximum time is about 5 to 6 seconds. The maximum production time for the cases with flow straightener can be as much as 27 seconds as is presented by the symmetric case. The symmetric case suffers a peculiar drop in the maximum production time at Reynolds number around 36,000. Similar drop is seen for the asymmetric case, but at higher Reynolds number. Nevertheless, the data pictured here is consistent with the finding in Figures 6 and 7 where the cases with flow straightener show higher power production. Interestingly here, the turbine's placement and Reynolds numbers seem to have minimum impact on the maximum time for the case without flow straightener. On the other hand, for the cases with flow straightener, the Reynolds numbers indicate strong influence on the maximum production time. The results for the case with flow straightener also suggests that the symmetric case shows higher maximum time than the asymmetric case, with the exception of the data at Reynolds number around 36,000. The reduction in production time could be explained by the closeness of the turbine to the chamber's wall. Visual observation during the experiments indicated that the narrow channel between the turbine and the wall reduces the amount of water flow on this side and that results in reduction of turbine's rotation. Based on our past works on the effects of upstream blockages [32, 38] , the asymmetric flow pattern was expected to promote autorotation. Similar phenomenon of increasing autorotation caused by upstream blockage was also reported in air channel passing by polygonal prisms [39]. But the asymmetric mechanism did not work here due to the significant reduction in the flowrates in the narrow channel between the turbine and the wall. Further studies on the effects of turbine's placement with respect to the symmetry line would have to be done on wider observation channel than the current one.

3.2 Results from Drag Experiments

The drag experiments result in the RPM and drag data. Specific for this drag experiment, the turbine is allowed to rotate relative to the fixed shaft, unlike the power experiments. A commercial 2-mm smooth stainless steel bearing is carefully press-fitted into the top side of the turbine. The 2-mm stainless steel shaft is covered by a 3d-printed rigid hollow cylinder to prevent bending caused

by force generated by water flow. The RPM data are reported in Figures 11 to 15 below. Figure 16 displays the outcomes from the drag experiment in terms of coefficient of drag or C_D.

The RPM results presented in Figures 11, 12, and 13 confirm positive exponential correlations between the Reynolds numbers and the rotational speed (RPM) of the turbine models. The correlations are made between the Reynolds numbers and the mean RPM data gathered for different depths for each Reynolds number. Figure 11 displays the outcome for turbine model with 5% infill tested at various depth. Results indicate the effects of the depth when the Reynolds numbers are higher than 30,000. The RPM is most affected when the turbine is placed at 7.5 and 9 cm. Figure 12 shows the RPM versus Reynolds numbers for turbine model with the 3d-printing infill of 40%. Generally, the outcome shows exponential trend of RPM with respect to the Reynolds numbers similar to that displayed in Figure 11. The exponential curve here is steeper than in Figure 11. Interestingly, here, the effects of depth cannot be easily appreciated. The data from the three depths are approximately the same for some Reynolds numbers and the RPM are approximately the same for all Reynolds numbers for two depths data.

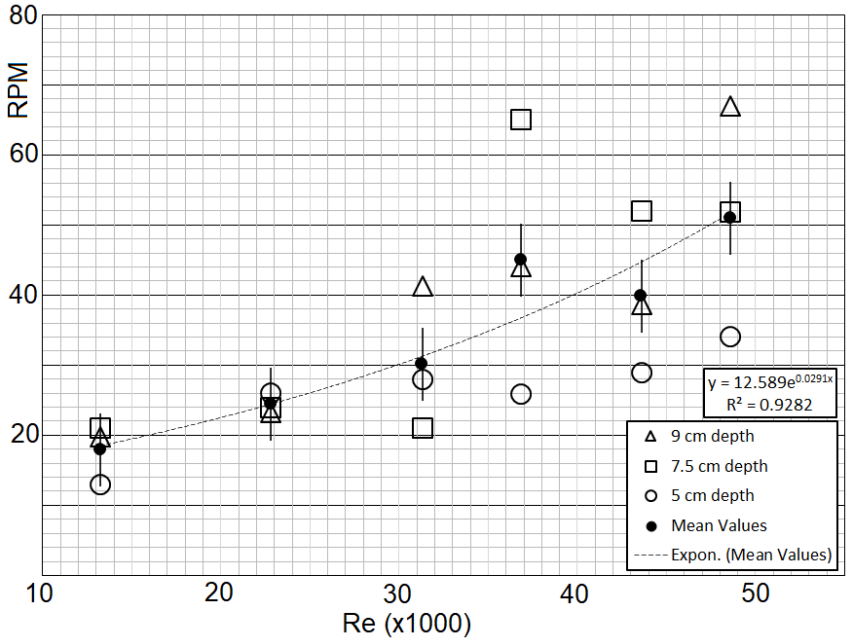

Figure 11. RPM values vs. Reynolds numbers for turbine model with 5% infill tested at different depths of 5 cm (circle), 7.5 cm (square), and 9 cm (triangle)

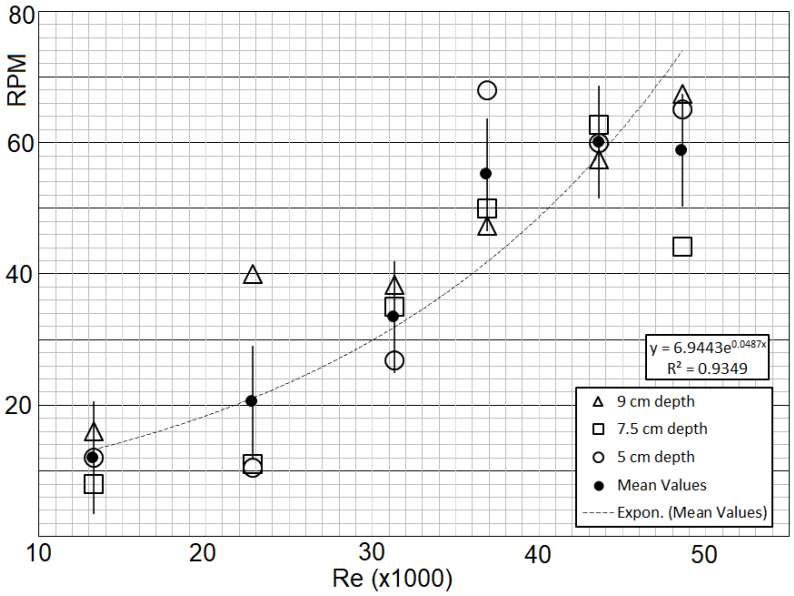

Figure 12. RPM values vs. Reynolds Number for 40% infill model tested at different depths of 5 cm (circle), 7.5 cm (square), and 9 cm (triangle)

The effects of the turbine's depth reappears in Figure 13, when the turbine model with 80% infills is used. Here, it can be seen that the RPM values for the three depths start to deviate after the Reynolds number of 30,000. Similar to results from turbine model with 5% infill, the RPM for turbine model with 80% infill placed 5 cm below the surface is the lowest at high Reynolds numbers.

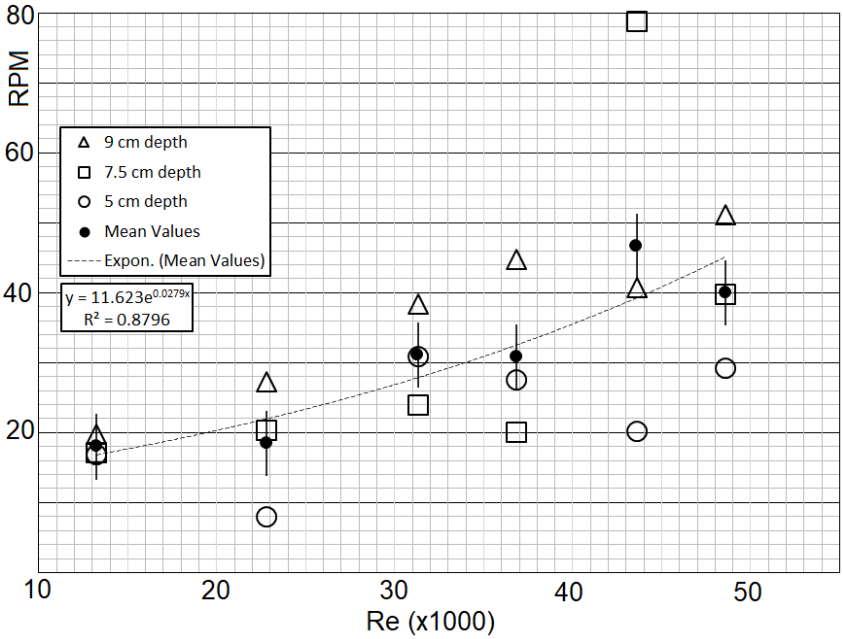

Figure 13. RPM values vs. Reynolds Number for 80% infill model tested at different depths of 5 cm (circle), 7.5 cm (square), and 9 cm (triangle)

When the RPM data for different depths are averaged, the effects of varying the infills can be seen in Figure 14. This figure suggests that the turbine model with 40% infill is optimal as it can provide the best RPM which leads to high power generation. The effects of the infills or mass can be seen when the Reynolds numbers are larger than 30,000. Nevertheless, the graph does not suggest infills with worst RPM. Both models with 5% and 80% infills also show increase in RPM with the increase in flow speed.

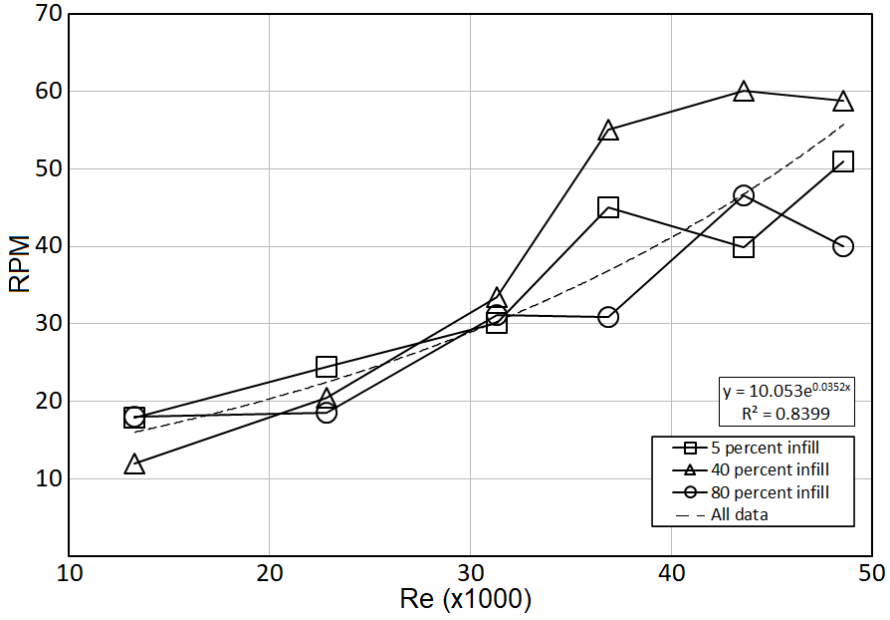

Figure 14. Mean RPM vs. Reynolds numbers for various 3d-printing infills parameters. The RPM data are averaged from three different depth data.

When the data for each infills are averaged according to their depth, the Figure 15 depicts the results. Here, it can be seen that all data indicate consistent growth with the increase of Reynolds numbers. The graph indicates weak influence of the depths as the RPM for each Reynolds number are not significantly difference. Again, at high Reynolds numbers, the effects are more pronounced than at low Reynolds numbers. Nevertheless, it can be suggested that the turbine's depth of 9 cm consistently results in high RPM.

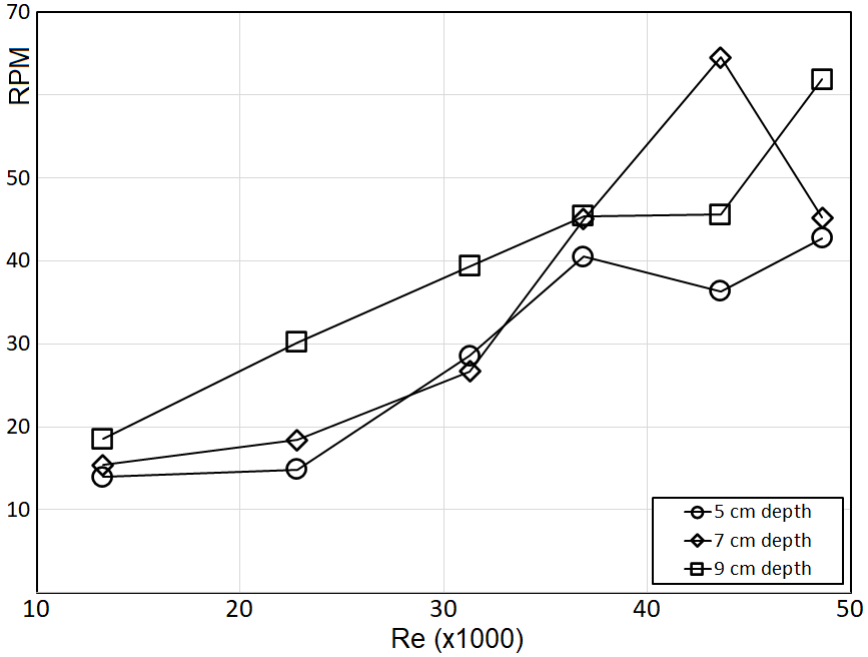

Figure 15. Mean RPM vs. Reynolds Number for each depth tested. The RPM data are averaged from various infills.

Figure 16 displays the coefficient of drag (C_D) calculated using the equation (2) above for the tested Reynolds numbers and infill parameters. The graph indicates nonlinear relationship between the C_D and the Reynolds numbers. As the flow speed increases, the C_D decreases in a nonlinear trend. The continuous force data were collected by the Vernier force sensor for 60 seconds. The accuracy of this measurement method has been discussed in our past work [30]. The drag forces used in the calculation have been deducted by the forces exerted on the 3d-printed hollow cylinder used to protect the 2-mm turbine shaft from bending. Time-averaged force values were used in the calculation of coefficient of drag. In the drag experiments, the turbine's depth is set at 9 cm from the water surface. The C_D was found to be in between a maximum of ~ 1.1, given by the lightest model with 5% infill, and minimum of ~ 0.21, given by the heaviest model with 80% infills. The C_D by the turbine models with 80% and 40% infills are essentially equal. We hypothesized that the light weight of the turbine with 5% infill has significant effects on the C_D at low Reynolds numbers. The effects of weight are diminished as the Reynolds numbers become large. Relating to the RPM results, we hypothesize that turbine models with high infill show less impulsive motion which leads to a smoother transition of fluid force into rotational inertia due to the vortex shedding of the models. The range of the C_D can be compared within reasonable margin errors to published values for long cylinders and square bars of 1.2 and 2.2, respectively [40]. The C_D values were also compared to that obtained from an empirical equation for cylinder, proposed by Tang et al.[41], that is valid for $10^4 \leq Re \leq 4.5 \times 10^5$.

$$C_D = -7.81 \times 10^{-18}\, Re^3 - 1.91 \times 10^{-12}\, Re^2 + 5.71 \times 10^{-7} Re + 1.15$$

Substituting the Reynolds numbers used in our experiments, the C_D are found to be in between 1.157 to 1.172. The values certainly are still higher than our findings, but the empirical formulation does not consider the length of the cylinder. Considering the model as a 3d-short cylinder, the

length-to-diameter ratio of the turbine is $\frac{L}{D} \sim 1$ and this corresponds to C_D value of 0.64 [40], which closely corresponds to our finding at high Reynolds numbers.

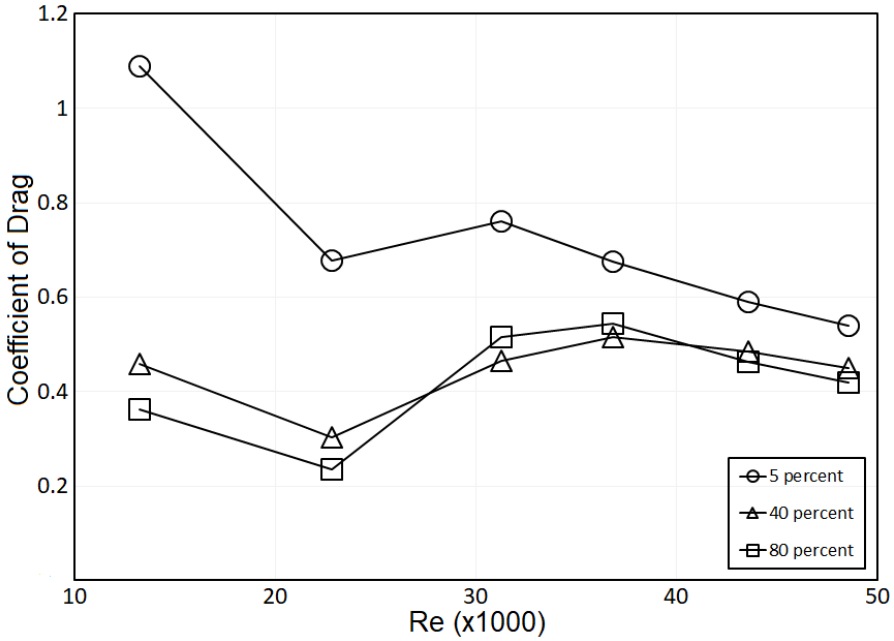

Figure 16. Coefficient of Drag curves for the Cross Cylinder turbine with various 3d-printing infill percentages tested for increasing Reynolds number. The low infill results in low printing density and light weight model. The data above shows the effect of low weight on the drag coefficient.

The results from the drag experiment corresponds well with data for the RPM in that it confirms the effectiveness of turbines with 40% infill. This turbine clearly shows minimal effects of weight in the C_D and provides the best RPM for the given range of Reynolds numbers. In future experiments, this may be an item to examine in more detail as this drag is undoubtedly decreasing maximum possible power production.

In summary, the presented data indicates the effects of flow speed, in terms of Reynolds numbers, on the power production, RPM, and drag. Experiment data also revealed the effects of placing an upstream flow straightener and turbine's placement in the stream on the power production. The presence of the flow straightener significantly increases the power production and efficiency in symmetric and asymmetric cases. The multiplier effect is presumably due to the local increase in the flow speed and the uniformity of the incoming flow. The power production is consistently increased with flow speed for turbine's placed in symmetric arrangement. However, for the asymmetric case, the power production shows a local maximum when the flow straightener was used. The low power production on asymmetric cases is hypothesized to be partly due to the closeness of one turbine's side to the chamber's wall. The narrow gap between the wall and the turbine side reduces the amount of flow necessary to provide torque. For all cases, the number of "flips" in the rotational direction and production time correlates well with the power production. The low number of flips corresponds to high power production. The current project presented power and RPM data of cross cylinder turbine models for higher range of Reynolds numbers than past studies [32, 38]. While the amount of power obtained in the current work is less than that produced in the past works, the increasing trend with the flow speed is very consistent. The multiplier effects produced by the flow straightener reflect the effects of upstream blockage on the power production presented in past works[32]. The small power production of the current work may be attributed to the utilization of a DC motor with high resistance. The RPM experiments revealed consistent increase of RPM with the Reynolds numbers in a nonlinear manner for various cases of turbine's densities and depth of placement. For Reynolds numbers around 28K to 34K, the current work shows less RPM than that demonstrated in the past work[32]. We hypothesize that the reduction is caused by the lack of uniform flow produced by a flow straightener embedded in

the commercial flow tank used in the past work. Unlike the setup used in the past work, here the turbine is designed to rotate on a fixed shaft in order to reduce friction. The drag experiment has resulted in data for rotating cross cylinder turbine that have not been available in the past. Results indicate that the C_D numbers are affected by the turbine's light weight. Comparing to published data on similar shapes, the C_D obtained in this work are in a good agreement. Data on the drag, along with RPM and power data, may guide better bladeless turbine designs.

4. Conclusion

In this paper, the drag measurement of the rotating bladeless cross-cylinder turbine model was shown for the first time for various Reynolds numbers, ranging from 13K to almost 50K. The drag coefficient seems to decrease with the increase in Reynolds number. The significant effects of upstream flow straightener were demonstrated in both power and efficiency. And it was also shown that the placement of turbine in the channel affects the performance and power production. In conclusion, experimentation involving variation of the flow speed or Reynolds number within the flow tank along with the implementation of factors that affect the power production continue to result in data useful for exploration of hydrokinetic energy from vortex-induced auto-rotating turbines.

References

[1] International Energy Agency (2021). Review 2021 Assessing the effects of economic recoveries on global energy demand and CO 2 emissions in 2021 Global Energy. Retrieved from www.iea.org/t&c/

[2] Ibrahim, W. I., Mohamed, M. R., Ismail, R. M. T. R., Leung, P. K., Xing, W. W., & Shah, A. A. (2021). Hydrokinetic energy harnessing technologies: A review. *Energy Reports*, *7*, 2021–2042. https://doi.org/10.1016/J.EGYR.2021.04.003

[3] Susilowati, Y., Irasari, P., & Susatyo, A. (2019). Study of Hydroelectric Power Plant Potential of Mahakam River Basin East Kalimantan Indonesia. *Proceeding - 2019 International Conference on Sustainable Energy Engineering and Application: Innovative Technology Toward Energy Resilience, ICSEEA 2019*, 207–213. https://doi.org/10.1109/ICSEEA47812.2019.8938641

[4] Setiawan, D. (2015). Potential Sites Screening for Mini Hydro Power Plant Development in Kapuas Hulu, West Kalimantan: A GIS Approach. *Energy Procedia*, *65*, 76–82. https://doi.org/10.1016/J.EGYPRO.2015.01.034

[5] Suntoro, A., Hantoro, R., & Nuari, L. S. (2019). Larona hydropower inlet canal flow analysis as potential hydrokinetic energy generation. *AIP Conference Proceedings*, *2088*(1), 030004. https://doi.org/10.1063/1.5095309

[6] Anyi, M., Kirke, B., & Ali, S. (2010). Remote community electrification in Sarawak, Malaysia. *Renewable Energy*, *35*(7), 1609–1613. https://doi.org/10.1016/j.renene.2010.01.005

[7] Tan, K. W., Kirke, B., & Anyi, M. (2021). Small-scale hydrokinetic turbines for remote community electrification. *Energy for Sustainable Development*, *63*, 41–50. https://doi.org/10.1016/J.ESD.2021.05.005

[8] Azrulhisham, E. A., Jamaluddin, Z. Z., Azri, M. A., & Yusoff, S. B. M. (2018). Potential Evaluation of Vertical Axis Hydrokinetic Turbine Implementation in Equatorial River. *Journal of Physics: Conference Series*, *1072*(1), 012002. https://doi.org/10.1088/1742-6596/1072/1/012002

[9] Behrouzi, F., Nakisa, M., Maimun, A., & Ahmed, Y. M. (2016, September 1). Renewable energy potential in Malaysia: Hydrokinetic river/marine technology. *Renewable and Sustainable Energy Reviews*. Elsevier Ltd. https://doi.org/10.1016/j.rser.2016.05.020

[10] Salleh, M. B., Kamaruddin, N. M., & Mohamed-Kassim, Z. (2018). Micro-hydrokinetic turbine potential for sustainable power generation in Malaysia. *IOP Conference Series: Materials Science and Engineering*, *370*(1), 012053. https://doi.org/10.1088/1757-899X/370/1/012053

[11] Badrul Salleh, M., Kamaruddin, N. M., & Mohamed-Kassim, Z. (2019). Savonius hydrokinetic turbines for a sustainable river-based energy extraction: A review of the technology and potential applications in Malaysia. *Sustainable Energy Technologies and Assessments*, *36*. https://doi.org/10.1016/j.seta.2019.100554

[12] Yakub, U., Nayeem, S. M., Golammostafa, S. M., & Samrat, N. (2014). An investigation on hydro kinetic energy and analyzing its potentiality in Bangladesh. *2014 2nd International Conference on Green Energy and Technology, ICGET 2014*, 45–49. https://doi.org/10.1109/ICGET.2014.6966659

[13] Baruah, A., Basu, M., & Amuley, D. (2021). Modeling of an autonomous hybrid renewable energy system for electrification of a township: A case study for Sikkim, India. *Renewable and Sustainable*

Energy Reviews, *135*, 110158. https://doi.org/10.1016/J.RSER.2020.110158
[14] Ali, F., Srisuwan, C., Techato, K., Bennui, A., Suepa, T., & Niammuad, D. (2020). Theoretical Hydrokinetic Power Potential Assessment of the U-Tapao River Basin Using GIS. *Energies 2020, Vol. 13, Page 1749*, *13*(7), 1749. https://doi.org/10.3390/EN13071749
[15] Olatunji, O. A. S., Raphael, A. T., & Yomi, I. T. (2018). Hydrokinetic energy opportunity for rural electrification in Nigeria. *International Journal of Renewable Energy Development*, *7*(2), 183–190. https://doi.org/10.14710/ijred.7.2.183-190
[16] Eme, L. C., Ulasi, J. A., Alade Tunde, A. I., & Odunze, A. C. (2019). Hydrokinetic turbines for power generation in Nigerian river basins. *Water Practice and Technology*, *14*(1). https://doi.org/10.2166/wpt.2019.001
[17] Masud, I. A., & Suwa, Y. (2018). Viability of hydro-kinetic turbine as an alternative for renewable energy harvesting in Nigeria. *Proceedings - 12th SEATUC Symposium, SEATUC 2018*. https://doi.org/10.1109/SEATUC.2018.8788852
[18] Niebuhr, C. M., van Dijk, M., Neary, V. S., & Bhagwan, J. N. (2019). A review of hydrokinetic turbines and enhancement techniques for canal installations: Technology, applicability and potential. *Renewable and Sustainable Energy Reviews*. https://doi.org/10.1016/j.rser.2019.06.047
[19] Kusakana, K. (2014). A survey of innovative technologies increasing the viability of micro-hydropower as a cost effective rural electrification option in South Africa. *Renewable and Sustainable Energy Reviews*. Elsevier Ltd. https://doi.org/10.1016/j.rser.2014.05.026
[20] Henrique da Costa Oliveira, C., de Lourdes Cavalcanti Barros, M., Alves Castelo Branco, D., Soria, R., & Cesar Colonna Rosman, P. (2021). Evaluation of the hydraulic potential with hydrokinetic turbines for isolated systems in locations of the Amazon region. *Sustainable Energy Technologies and Assessments*, *45*, 101079. https://doi.org/10.1016/J.SETA.2021.101079
[21] Bárcenas Graniel, J. F., Fontes, J. V. H., Gomez Garcia, H. F., & Silva, R. (2021). Assessing Hydrokinetic Energy in the Mexican Caribbean: A Case Study in the Cozumel Channel. *Energies 2021, Vol. 14, Page 4411*, *14*(15), 4411. https://doi.org/10.3390/EN14154411
[22] Erinofiardi, Gokhale, P., Date, A., Akbarzadeh, A., Bismantolo, P., Suryono, A. F., … Nuramal, A. (2017). A Review on Micro Hydropower in Indonesia. *Energy Procedia*, *110*, 316–321 https://doi.org/10.1016/J.EGYPRO.2017.03.146
[23] VanZwieten, J., McAnally, W., Ahmad, J., Davis, T., Martin, J., Bevelhimer, M., … Trudeau, M. (2014). In-Stream Hydrokinetic Power: Review and Appraisal. *Journal of Energy Engineering*, *141*(3), 04014024. https://doi.org/10.1061/(ASCE)EY.1943-7897.0000197
[24] Fernandes, A. C., & Bakhshandeh Rostami, A. (2015). Hydrokinetic energy harvesting by an innovative vertical axis current turbine. *Renewable Energy*, *81*, 694–706 https://doi.org/10.1016/j.renene.2015.03.084
[25] Shao, N., Lian, J., Liu, F., Yan, X., & Li, P. (2020). Experimental investigation of flow induced motion and energy conversion for triangular prism. *Energy*, *194*, 116865. https://doi.org/10.1016/j.energy.2019.116865
[26] Soti, A. K., Thompson, M. C., Sheridan, J., & Bhardwaj, R. (2017). Harnessing electrical power from vortex-induced vibration of a circular cylinder. *Journal of Fluids and Structures*, *70*, 360–373 https://doi.org/10.1016/j.jfluidstructs.2017.02.009
[27] Lugt, H. J. (1983). Autorotation. *Annual Review of Fluid Mechanics*, *15*(1), 123–147 https://doi.org/10.1146/annurev.fl.15.010183.001011
[28] Riabouchinsky, D. P. (1935). Thirty Years of Theoretical and Experimental Research in Fluid Mechanics. *The Journal of the Royal Aeronautical Society*, *39*(292), 282–348. https://doi.org/10.1017/s0368393100112039
[29] Rostami, A. B., & Armandei, M. (2017, April 1). Renewable energy harvesting by vortex-induced motions: Review and benchmarking of technologies. *Renewable and Sustainable Energy Reviews*. Elsevier Ltd. https://doi.org/10.1016/j.rser.2016.11.202
[30] Wulandana, R. (2021). Open Water Flume for Fluid Mechanics Lab. *Fluids*, *6*(7), 242. Retrieved from https://doi.org/10.3390/fluids6070242
[31] Araneo, J., Chung, B. J. B. J., Cristaldi, M., Pateras, J., Vaidya, A., & Wulandana, R. (2019). Experimental control from wake induced autorotation with applications to energy harvesting. *International Journal of Green Energy*, *16*(15), 1400–1413 https://doi.org/10.1080/15435075.2019.1671413
[32] Wulandana, R., Foote, D., Vaidya, A., & Chung, B. J. (2021). Vortex-Induced Autorotation Potentials of Bladeless Turbine Models. *International Journal of Green Energy*, *Accepted 2*(Published online Jul 10 2021). Retrieved from https://doi.org/10.1080/15435075.2021.1941044
[33] Chung, B., Cohrs, M., Ernst, W., Galdi, G. P., & Vaidya, A. (2015). Wake--cylinder interactions of a

hinged cylinder at low and intermediate Reynolds numbers. *Archive of Applied Mechanics*, *86*(4), 627–641. https://doi.org/10.1007/s00419-015-1051-2

[34] Skews, B. W. (1991). Autorotation of many-sided bodies in an airstream. *Nature*, *352*(6335), 512–513. https://doi.org/10.1038/352512a0

[35] Khan, M. J., Bhuyan, G., Iqbal, T., Quaicoe, J. E., Iqbal, M. T., & Quaicoe, J. E. (2009). Hydrokinetic Energy Conversion Systems and Assessment of Horizontal and Vertical Axis Turbines for River and Tidal Applications: A Technology Status Review. *Applied Energy*, *86*(10), 1823–1835 https://doi.org/10.1016/j.apenergy.2009.02.017

[36] Khan, M. J., Iqbal, T., Quaicoe, J. E., Iqbal, M. T., & Quaicoe, J. E. (2008). River current energy conversion systems: Progress, prospects and challenges. *Renewable and Sustainable Energy Reviews*, *12*(8), 2177–2193. https://doi.org/10.1016/j.rser.2007.04.016

[37] Vernier. (n.d.). Go Direct® Force and Acceleration Sensor User Manual – Vernier. Retrieved June 7, 2021, from https://www.vernier.com/manuals/gdx-for/

[38] Araneo, J., Chung, B. J., Cristaldi, M., Pateras, J., Vaidya, A., & Wulandana, R. (2019). Experimental control from wake induced autorotation with applications to energy harvesting. *International Journal of Green Energy*, *16*(15). https://doi.org/10.1080/15435075.2019.1671413

[39] Skews, B. W. (1998). Autorotation of polygonal prisms with an upstream vane. *Journal of Wind Engineering and Industrial Aerodynamics*, *73*(2), 145–158. https://doi.org/10.1016/S0167-6105(97)00280-8

[40] White, F. M. (n.d.). *Fluid Mechanics* (7th ed.). New York: McGraw Hill.

[41] Tang, H., Tian, Z., Yan, J., & Yuan, S. (2014). Determining drag coefficients and their application in modelling of turbulent flow with submerged vegetation. *Advances in Water Resources*, *69*, 134–145. https://doi.org/10.1016/j.advwatres.2014.04.006